BMC Cancer

RESEARCH

Open Access

Photodynamic therapeutic activity of novel porphyrins against lung squamous cell carcinoma

Hao Meng[1†], Ren-Quan Ding[1†], Lei Jia[2], Xiang-peng Chen[1,3], Yu-hang Hu[1], Shu-min Wang[1*], Si-qi Lv[4*] and Fan Feng[5*]

Abstract

Porphyrins, as drug-food homologous bioactive substances, hold significant potential in nanomedicine research and photodynamic therapy (PDT). In this study, we synthesized two novel porphyrin compounds, PTA and PTBA, based on the porphyrin compound TCPP. Using these compounds, we prepared metal-porphyrin nanoparticles and evaluated their properties. Results from multiple assays demonstrated that both PTA and PTBA exhibited significantly enhanced photodynamic therapeutic activation under laser irradiation compared to TCPP. This included improved reactive oxygen species (ROS) and singlet oxygen release, as well as superior antitumor activity. When prepared as metal-porphyrin nanoparticles, all three compounds—PCN224 (TCPP with Zr^{4+}), PMOF01 (PTA with Zr^{4+}), and PMOF02 (PTBA with Zr^{4+})—showed significantly upregulated photodynamic therapeutic effects. These nanoparticles induced the accumulation of ROS and singlet oxygen in lung squamous cell carcinoma (LSCC) cells and demonstrated both in vitro and in vivo antitumor activity under laser irradiation. Notably, PMOF01 and PMOF02 exhibited much stronger antitumor effects compared to PCN224 in LSCC cells. Our findings highlight the photodynamic therapeutic potential of these novel porphyrin compounds and their nanoparticles. These results not only expand our understanding of porphyrins' antitumor capabilities but also provide new options for PDT applications.

Keywords Porphyrins, Photodynamic therapy, Porphyrin-metal nanoparticles, Lung squamous lung cancer, Antitumor activation

[†]Hao Meng and Ren-Quan Ding equality contribute to this work.

*Correspondence:
Shu-min Wang
sureman2003congo@163.com
Si-qi Lv
lvsiqi2024@163.com
Fan Feng
fengfanbio@126.com
[1]Department of Thoracic Surgery, General Hospital of Northern Theater Command, No.83, Wenhua Road, Shenhe District, Shenyang City, Liaoning province 110011, P.R. China
[2]Department of Health Service Training Center, The 32183 Military Hospital of PLA, No.81, Haiming Road, Taobei District, Baicheng City 137000, Liaoning province, P.R. China
[3]Graduate Training Base of General Hospital of Northern Theater Command of Dalian Medical University, Shenyang City, Liaoning province 110011, P.R. China
[4]Department of General &Thoracic Surgery, The 32183 Military Hospital of PLA, No.81, Haiming Road, Taobei District, Baicheng City, Liaoning province 137000, P.R. China
[5]Department of Laboratory Medicine, The Fifth Medical Center of Chinese PLA General Hospital, Beijing 100039, P.R. China

Introduction

Currently, due to the high prevalence of smoking across various age groups, intensifying air pollution, and increased life expectancy, lung cancer has become the most serious malignancy in China, with the highest number of cases and deaths [1, 2]. Lung cancer can be divided into the following pathological subtypes: non-small cell lung cancers (NSCLC); small cell lung cancer (SCLC) and rare cases, such as lymphocytoma and lung metastases from other malignant tumors [3 NSCLC is the most common pathologic subtype of lung cancer [1–3]. Within NSCLC, lung adenocarcinoma (LA) is not only a major subtype but also a focus of NSCLC research. Compared to LA, lung squamous carcinomas (LSCC) vary in histologic features, pathologic characteristics, and prognosis, and have relatively limited therapeutic options [4–5]. Currently, surgical treatment is still effective for LSCC [6–8]. For patients who cannot undergo surgery, such as those with progressive lung squamous cell carcinoma (LSCC), treatment strategies include molecular targeted therapy, radiofrequency ablation therapy, and chemotherapy [6–8]. However, the prognosis for LSCC patients remains unsatisfactory. Research to discover therapeutic strategies suitable for LSCC holds significant value.

Photodynamic therapy (PDT) is currently an effective and innovative antitumor therapy, offering the advantages of non-invasiveness, high efficiency, low toxicity, and good targeting [9–11]. During PDT, specific photosensitive materials absorb energy from a laser of a certain frequency and transfer it to surrounding molecules, generating cytotoxins like reactive oxygen species (ROS) or singlet oxygen ([1] O_2) to kill tumor cells [12, 13]. PDT's many advantages, including its noninvasive nature, have great theoretical and practical significance, but further exploration is needed to achieve safer and more effective treatment [14, 15].

Porphyrins are a large class of substances found in both medicine and food [16, 17]. For instance, porphyrin-cobalt is vitamin B12, and porphyrin-magnesium is chlorophyll [18, 19]. Porphyrin iron is particularly significant in the context of iron deficiency anemia [20, 21]. Additionally, porphyrin compounds can serve as high-value photosensitizers and nutritional supplements [22]. TCPP, a representative porphyrin compound, is commonly used in photodynamic therapy (PDT) and holds great research potential [23, 24]. While TCPP may not be potent enough as a photosensitizer on its own, it can form nanoparticles through ligand bonding with metal ions (a capability not shared by other porphyrin compounds) [25]. These metal ions significantly enhance TCPP's antitumor activity under laser irradiation [25]. However, TCPP has drawbacks such as poor photostability, water solubility, biocompatibility, and weak near-infrared (NIR) absorption. Modifying or re-synthesizing TCPP's structure is crucial to overcoming these shortcomings and improving PDT's effectiveness.

Lung squamous cell carcinoma (LSCC) is an ideal target for PDT treatment. Deep tumors in general visceral organs are challenging to treat with PDT, but LSCC tumors are typically located in the trachea, making it feasible to directly irradiate them with a laser probe under bronchoscopic guidance [26, 27]. Thus, studying PDT in LSCC is of great significance. In this study, TCPP was structurally modified by introducing phenyl or triphenylamine structures to enhance conjugation within the porphyrin structure and π-π stacking. This led to the successful preparation of new porphyrin compounds, PTA and PTBA, which exhibited superior photopotentiostimulatory activities compared to TCPP. PTA, PTBA, and TCPP were also found to be highly effective in treating LSCC and capable of forming nanoparticles with 4-valent chromium ions, which possess good photosensitivity. These nanoparticles were named PCN224, PMOF1, and PMOF2. Among them, PMOF1 exhibited the best activity, significantly outperforming PCN224. This study has thus identified a new and superior porphyrin compound, PTA, which could provide new insights into the research of PDT for lung squamous cell carcinoma.

Materials and methods

Cell lines and agents

Three types of porphyrin compounds were involved in this study: tetrakis(4-carboxyphenyl)porphyrin (TCPP-20), PTBA, and PTA. TCPP-20 and PTBA/PTA (with PTBA or PTA obtained through chemical synthesis) were purchased from Beijing InnoChem Science & Technology Co., Ltd. Additional chemical reagents, including benzoic acid, zirconium chloride ($ZrCl_4$), 1-diphenylisobenzofuran (DPBF), 2,7-dichlorofluorescein diacetate (DCFH-DA), dimethyl sulfoxide (DMSO), and N-dimethylformamide (DMF), were also purchased from Beijing InnoChem Science & Technology Co., Ltd. Phosphate buffer solution (PBS), Dulbecco's Modified Eagle Medium (DMEM), and fetal bovine serum were sourced from Gibico (Gibico™, a brand of ThermoFisher Scientific, Waltham, Massachusetts, USA). The AnnexinV-FITC/DAPI apoptosis kit was purchased from Beyotime Biotech, Inc., and the ROS detection kit was obtained from the same company.

The research utilized various human superficial tumor cell lines, including: Thyroid cancer cell lines: MTC cell line TT, bht-101, KTC-1, and B-CPAP; Esophageal squamous cell carcinoma (ESCC) cell lines: KYSE70, KYSE140, and KYSE450; Breast cancer cell lines: MDA-MB-231, MCF-7, and BT474; Skin cancer cell line: A-431; Melanoma cell lines: A-375 and SK-MEL-1; Lung cancer cell lines: squamous cell carcinoma (H520), large cell lung cancer (H460), adenocarcinoma (A549), and small cell

lung cancer (H446); Hepatocellular carcinoma cell line: HepG2; Colorectal cancer cell lines: LoVo and SW480; These cell lines were purchased from the National Infrastructure of Cell Line Resources, Chinese Academy of Medical Sciences / Peking Union Medical College and were preserved and cultured in our laboratory.

Chemical synthesis of novel porphyrin compounds and Preparation of metal nanoparticles

Synthesis of porphyrin compound PTA

To synthesize the porphyrin compound PTA (3,3',3",3"'-((9E,10Z,14Z,16E,19Z)-5 H,6 H-porphyrin-5,10,15,20-tetrayl)tetrabenzoic acid), 5 g of methyl 3-formylbenzoate were dissolved in 70 milliliters of propionic acid and heated to 120 °C. A solution of 2.1 g of pyrrole in propionic acid was added dropwise to the reaction mixture, which was then refluxed for 12 h. After cooling to room temperature, a purple precipitate was collected, yielding 782 milligrams of product. Subsequently, 300 milligrams of the por-m2 compound were dissolved in a mixed solvent of 10 milliliters of tetrahydrofuran and 10 milliliters of methanol, and 10 milliliters of an aqueous solution containing 1.06 g of potassium hydroxide were added. The reaction mixture was refluxed for 10 h and then cooled to room temperature. The precipitate was collected and purified by column chromatography using a dichloromethane–methanol mixture (v/v ratio of 50:1), yielding a purple solid product (52 mg). Spectral analysis (1 H NMR, 400 MHz, DMSO-d6) showed peaks at δ 8.85 (d, 8 H), 8.58–7.90 (m, 16 H), and – 2.90 (s, 2 H). Figure 1A illustrates the chemical synthesis route of PTA.

Synthesis of porphyrin compound PTBA

To synthesize the porphyrin compound PTBA (4',4",4"",4"""-((9E,10Z,14Z,16E,19Z)-5 H,6 H-porphyrin-5,10,15,20-tetrayl)tetrakis(([1,1'-biphenyl]-4-carboxylic acid))), 500 milligrams of (1Z,4Z,6E,15Z,19E)-5,10,15,20-tetrakis(4-bromophenyl)-9 H,10 H-porphyrin and 850 milligrams of methyl 4-(4,4,5,5-tetramethyl-1,3,2-dioxaborolan-2-yl)benzoate were dissolved in 100 milliliters of tetrahydrofuran. Potassium hydroxide (1.05 g) and palladium(0) tetrakis(triphenylphosphine) (80 milligrams) were added to the solution. Under nitrogen protection, the reaction mixture was refluxed for 10 h. After cooling, the reaction mixture was filtered, concentrated, and purified by column chromatography, yielding 80 milligrams of a purple solid product. Next, 80 milligrams of the por-m5 compound were dissolved in 15 milliliters of methanol, and 125 milligrams of sodium hydroxide were added. The reaction mixture was refluxed for 8 h, then cooled, and the organic solvent was evaporated. The purple solid product was ultimately obtained via column chromatography using a dichloromethane–methanol mixture (v/v ratio of 80:1). Spectral analysis (1 H NMR, 400 MHz, DMSO-d6) showed peaks at δ 8.98 (s, 8 H), 8.56–7.76 (m, 32 H), and – 2.81 (s, 2 H). Figure 1B illustrates the chemical synthesis route of PTBA.

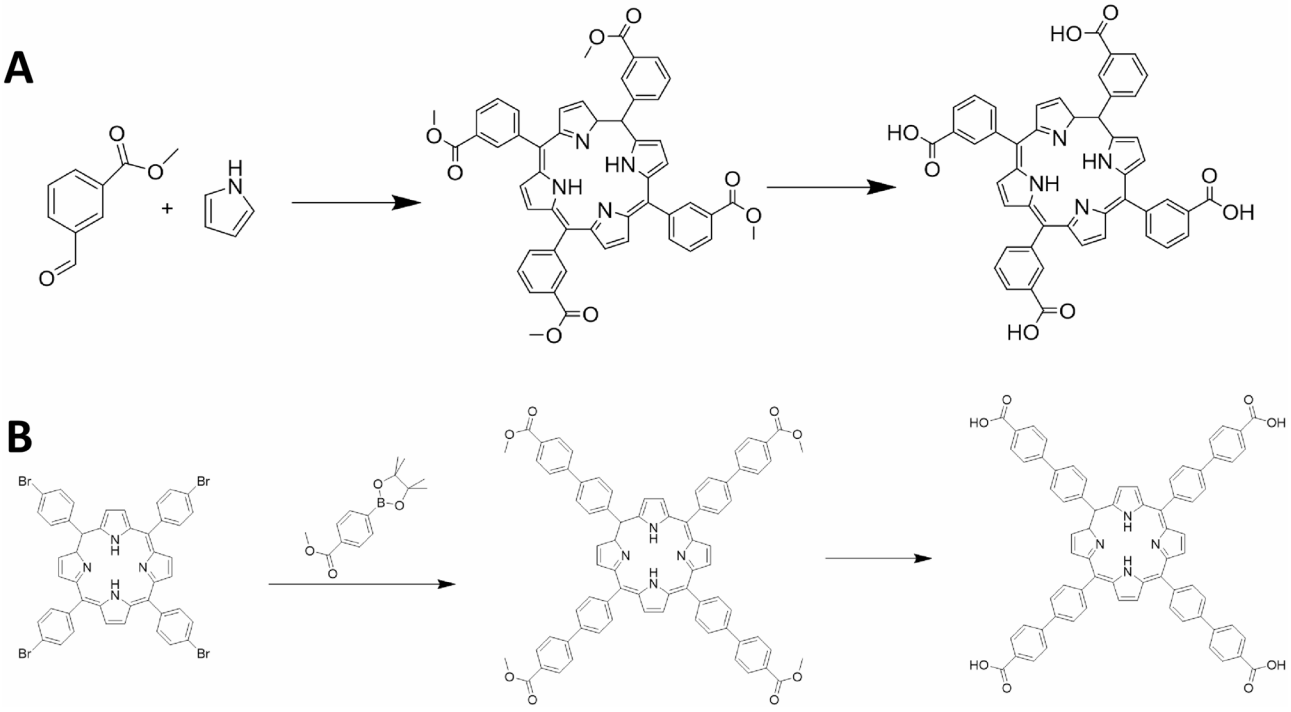

Fig. 1 Chemical Synthetic Routes of PTA and PTBA. (**A**) Chemical synthetic routes of PTA. (**B**) Chemical synthetic routes of PTBA

Preparation and characterization of metal nanoparticles based on novel porphyrin compounds

To synthesize metal nanoparticles based on porphyrin compounds, 30 milligrams of zirconium oxychloride octahydrate and 280 milligrams of benzoic acid were dissolved in 10 milliliters of dimethylformamide (DMF) with vigorous stirring at room temperature. After 30 min of stirring, 0.5 milliliters of a solution containing 20 milligrams per milliliter of TCPP, PTA, or PTBA in DMF were added dropwise to the mixture, which was then heated to 90 °C for 5 h. After cooling, purple nanoparticles were obtained by centrifugation for 30 min at 12,000 rpm, rinsed three times with DMF, and dispersed in 2 milliliters of DMF for further use. The metal nanoparticles prepared using TCPP, PTA, and PTBA were named PCN224, PMOF1, and PMOF2, respectively.

Analysis of physical and chemical properties of prepared porphyrin metal nanoparticles

The nanoparticles, PCN224, PMOF1, and PMOF2, were characterized using various techniques:

PXRD (Powder X-ray diffraction); SEM (Scanning Electron Microscope) (MIRA LMS, TESCAN, Brno-Kohoutovice, Czech Republic); DLS (Dynamic Light Scattering); BET (Brunauer-Emmett-Teller) analysis with the ASAP 2460 detector (Micromeritics, Norcross, GA, U.S.A.); Zeta potential tests with the Zetasizer Nano ZS90 detector (Malvern, UK). The morphology of these nanoparticles was examined using the SEM. The specific surface area and porosity were measured with the ASAP 2460 detector. The nanoparticle size and zeta potential were determined using the Zetasizer Nano ZS90.

Additional characterizations included: Fourier Transform Infrared Spectrometer (FTIR) using the Spectrum GX detector (PerkinElmer, Waltham, USA); UV-Vis absorption spectra recorded by the LAMBDA750s spectrometer (PerkinElmer, Waltham, USA). Fluorescence spectra recorded with the LS-55 fluorometer (PerkinElmer, Waltham, USA); Crystallographic information (XRD) obtained using the SmartLab3 X-ray diffractometer (Rigaku, Japan). This comprehensive analysis provided detailed insights into the physical and chemical properties of the nanoparticles.

Detection of ROS and singlet oxygen levels

For the prepared nanoparticles, the levels of singlet oxygen (O_2) and reactive oxygen species (ROS) generated by laser irradiation were investigated in both cell-free systems and within cells.

Detection of $^1O_2$ in a cell-free system

The fluorescent probe DPBF was used to quantify O_2 levels. A 0.5 mmol/L solution of DPBF in Dimethyl Sulfoxide (DMSO) was prepared in the dark. The nanoparticle sample was diluted to 0.01 mmol/L in DMSO, with pure DMSO serving as a control. In a cuvette, 3 mL of DMSO was mixed with 0.1 mL of the DPBF solution in the dark. Subsequently, 0.05 mL of the sample solution was added and thoroughly mixed in the dark. The mixture was then irradiated with a 660 nm laser at an intensity of 100 mW/cm² for 10 min. The absorption curves of the solutions were monitored at intervals of 1 to 10 min post-irradiation, with absorbance values at 414 nm measured to generate absorbance curves. The release profile of 1O2 was determined by analyzing the relative change in absorbance of the samples.

Detection of ROS in a cell-free system

DCFH-DA was selected as the fluorescent probe to detect ROS generation. A 1 mmol/L solution of DCFH-DA was diluted to 0.05 mmol/L with DMSO and then further diluted with PBS to a total volume of 10 mL. In a cuvette, 0.1 mL of the nanoparticle solution was mixed with 2.9 mL of the DCFH-DA solution. Each group was irradiated with a 660 nm laser at an intensity of 100 mW/cm² for 10 min, and the absorption levels were evaluated at intervals of 1 to 10 min post-exposure. A PBS solution of DCFH-DA served as a blank control. The fluorescence intensity variations within the wavelength range of 500–560 nm were measured for each sample (Control, PCN224, PKI@PCN224, and F68-PKI@PCN224) at various time points. Subsequently, the release curves of ROS were plotted.

Detection of ROS in cells

The LSCC cell line H520 was cultured and inoculated onto confocal dishes. After 24 h of treatment with 100 μmol/L concentrations of PCN224, PMOF1, or PMOF2, a 10 μmol/L solution of the DCFH-DA probe was introduced and incubated for 30 min. The cells were then irradiated with a 660 nm laser at an intensity of 100 mW/cm² for 10 min. Subsequently, the cells were fixed with 4% paraformaldehyde in PBS, permeabilized with 0.5% Triton-X-100 in PBS, and observed or photographed using a confocal microscope. The nucleus was labeled with Hoechst 33,342 dye. During fluorescence imaging, blue fluorescence was excited using ultraviolet light (excitation wavelength 350 nm, emission wavelength 460 nm), and green fluorescence was excited using blue light (excitation wavelength 460 nm, emission wavelength 590 nm). The results were displayed as fluorescent images, with blue fluorescence indicating the nucleus and green fluorescence indicating ROS in the cytoplasm. Quantitative analysis of the obtained images was performed using ImageJ software.

Cellular uptake experiments and tissue retention examination

Cellular uptake assay

The cellular uptake assay aimed to investigate whether porphyrins prepared as nanoparticles could enhance the cellular uptake of these compounds. LSCC H520 cells were cultured and prepared as a single-cell suspension. These cell suspensions were then inoculated into 6-well plates and incubated at 37 °C for 24 h. The cells were treated with a 100 μmol/L dose of TCPP, PTA, PTBA, PCN224, PMOF1, or PMOF2. The cells were harvested at specific time points (0, 2, 4, 8, 12, 24, or 48 h) [25]. The intracellular contents of TCPP, PTA, and PTBA were analyzed using LC-MS/MS (Liquid Chromatograph Mass Spectrometer).

Tissue retention examination

The tissue retention examination was conducted to assess whether the preparation of porphyrin compounds as nanoparticles could improve or affect their local retention in tumor tissues. In this experiment, TCPP, PTA, PTBA, PCN224, PMOF1, and PMOF2 were prepared as a 10 mg/ml solution. LSCC cells were subcutaneously seeded in nude mice to form subcutaneous tumors. When the tumor volume reached approximately 500 mm^3, TCPP, PTA, PTBA, PCN224, PMOF1, and PMOF2 were directly injected into the tumor tissue with a volume of about 20 μl. The tumor tissue was collected at various time points (0, 6, 12, 24, 48, or 72 h) [28, 29]. The intra-tumor tissue contents of TCPP, PTA, and PTBA were analyzed using LC-MS/MS.

LC-MS/MS assay procedure

For the LC-MS/MS assays, cell samples from each group (Including both the porphyrin compound group and the nanoparticle group) were collected, resuspended in PBS, and then mixed with approximately twice the volume of acetonitrile. Tumor tissue was homogenized and resuspended in PBS, followed by the addition of acetonitrile for extraction. The samples were vortexed for 15 min to extract TCPP, PTA, and PTBA, and then centrifuged at 12,000 revolutions per minute at 4 °C. The materials separated into three layers: aqueous phase, organic phase, and cellular debris. The organic phase was used for LC-MS/MS analysis. The overall drug concentration was determined based on the dosage and volume of drug administered to the cells. The LC-MS/MS assay results were used to quantify the amount of TCPP, PTA, and PTBA in the samples.

Whether PCN224, PMOF1, or PMOF2, these materials fundamentally consist solely of porphyrins (TCPP, PTA, or PTBA) coordinated with metal ions. Therefore, the quantification of these metal-organic nanoparticles essentially measures the porphyrin compounds (TCPP derivatives) themselves (in all samples, the porphyrin components [TCPP, PTA or PTBA] were extracted into acetonitrile, while metal ions remained in the aqueous phase). For both cellular uptake experiments and tumor tissue retention studies, we conducted parallel testing using either free porphyrin compounds or nanoparticles at equimolar porphyrin concentrations. The analytical method for nanoparticles was thus identical to that for free porphyrins - both were quantified via LC-MS/MS detection of the porphyrin components.

In vitro antitumor activation examination

The in vitro antitumor activation was evaluated using MTT, colony formation, and apoptosis assays.

MTT assays

For MTT assays, cells were cultured in DMEM (complete Dulbecco's modified Eagle's medium) supplemented with 10% FBS (fetal bovine serum) at 37 °C in a 5% CO_2 environment. The cells were prepared as a single-cell suspension and seeded into 96-well plates at a density of 8,000 cells per well in 100 μl of cell suspension. The plates were incubated for 24 h at 37 °C. Subsequently, the cells were treated with various concentrations of TCPP, PTA, PTBA, PCN224, PMOF1, or PMOF2 for 48 h, either with or without exposure to a laser with a wavelength of 660 nm and a power of 100 mW/cm^2 for five minutes. The non-irradiated group was cultured in the absence of light. After treatment, the cells were harvested and subjected to the MTT assay following the manufacturer's instructions (Amresco, Cleveland, OH, USA). The optical density (OD) at 490 nm was used to reflect the relative number of surviving cells. The inhibition rate was calculated as ((OD 490 nm in control group - OD 490 nm in drug-treated group) / OD 490 nm in control group) × 100% and plotted into heatmaps [30]..

Colony formation assays

For colony formation assays, H520 cells were cultured in DMEM supplemented with 10% FBS at 37 °C in a 5% CO_2 environment. The cells were prepared as a single-cell suspension and seeded into 6-well plates at a density of 1×10^6 cells per well in 1 ml of cell suspension. The plates were incubated for 24 h at 37 °C. Subsequently, the cells were treated with a 100μmol/L dose of TCPP, PTA, PTBA, PCN224, PMOF1, or PMOF2 for 48 h, either with or without exposure to a laser with a wavelength of 660 nm and a power of 100 mW/cm^2 for five minutes. After treatment, the cells were collected, and approximately 2,000 cells in single-cell suspension were seeded into each well of a new 6-well plate. The plate was then incubated continuously at 37 °C with 5% CO_2. After 3–4 weeks, the colonies were fixed with 4% paraformaldehyde and stained with a 1.5% crystal violet solution [31]. The

images of the colonies were quantitatively analyzed using Image J software (National Institutes of Health, Bethesda, MD, USA), and the relative number of colonies (folds of control) was calculated based on the total area of each colony [31]. During this step of ImageJ software analysis, the photographs of 6-well plates were first imported into ImageJ and converted to pure black-and-white images. Subsequently, by manually adjusting the contrast, all colonies in each photograph were outlined. The following parameters were then determined: (1) the number of colonies, and (2) the total area of colonies. As a supplementary analysis, crystal violet adsorbed by cell colonies in the 6-well plates was dissolved using absolute ethanol, followed by absorbance measurement (O.D. 590 nm). Finally, the relative fold change of each group was calculated with the control group normalized to 1.

Apoptosis assays

For apoptosis assays, H520 cells were seeded into 6-well plates. The cells were treated with a 100 μmol/L dose of TCPP, PTA, PTBA, PCN224, PMOF1, or PMOF2 for 48 h, either with or without exposure to a laser with a wavelength of 660 nm and a power of 100 mW/cm² for five minutes. Apoptosis was detected using the Annexin V/7-AAD double staining method from BD's apoptosis assay kit (Cat. No.: 559763; Becton, Dickinson and Company, Franklin Lakes, NJ, USA). Cell fixation and permeabilization were performed according to the manufacturer's instructions. The cells were stained with 7-AAD, Annexin V alone, or double-stained and then analyzed using flow cytometry. The results were presented as apoptosis plot images, where Annexin V single-positive cells indicated early apoptosis, and 7-AAD single-positive cells indicated late apoptosis [32]. The total number of apoptotic cells in each group was the sum of early and late apoptosis. Image J software was used to analyze the tumor growth curve graph and perform quantitative analysis based on the area under each curve.

In vivo antitumor activation

Nude mouse models were used to examine the in vivo antitumor activity of the nanoparticles and purchased from Si-Bei-Fu Corporation, Beijing China. The experimental animals were female nude mice aged 4–5 weeks, housed under SPF conditions. H520 cells were cultured and injected subcutaneously into each mouse. Each animal received an inoculation of cells once (5×10^6 cells per mouse) to form a subcutaneous tumor tissue. Subsequently, drug administration experiments (PCN224, PMOF1, and PMOF2) were conducted. Tail vein injection and intratumoral injection were the methods used for administration in this study. For the tail vein injection experiment, when the tumor volume reached approximately 500 mm³, the mice received PCN224, PMOF1, or PMOF2 via tail vein injection (low dose: 0.5 mg/kg; high dose: 5 mg/kg). This was followed by laser irradiation (100 mW/cm² for 10 min) of the subcutaneous tumor tissue. A precision balance was used to measure tumor weight, and the formula V = (tumor length) × (tumor width)² / 2 was used to calculate the tumor volume at each time point. Tumor weights were presented as bar charts with mean ± SD. Tumor growth curves were obtained based on tumor volumes at each time point. Body weights, weights of major organs, and major blood markers were determined using methods reported in previous publications [33, 34]..

For the intratumoral injection experiment, when the tumor volume reached approximately 500 mm³, about 20 μl of drug solution (10 mg/ml) (PCN224, PMOF1, or PMOF2; 20 μg for low dose and 200 μg for high dose) was injected directly into the tumor tissue. This was followed by laser irradiation (100 mW/cm² for 10 min) of the subcutaneous tumor tissue. For the euthanasia/sacrifice methods, the nude mice were anaesthetised and/or unconscious. The detailed methods were: the nude mice were anesthetized using an anesthesia machine with isoflurane as the inhalation anesthetic. Initially, 1.5% v/v (volume/volume concentration, standard in anesthesia protocols) isoflurane was administered to induce anesthesia in the nude mice. Once the mice were unconscious, anesthesia was maintained with 0.5% v/v isoflurane. The mice were then euthanized by cervical dislocation to collect subcutaneous tumor tissues.

Tumor weight was measured using a precision balance, and the same formula was used to calculate the tumor volume at the indicated time points. Tumor weights were presented as bar charts with mean ± SD. Tumor growth curves were obtained based on tumor volumes at each time point. Body weights, weights of major organs, and major blood markers were determined using methods reported in previous publications. ImageJ software was used to analyze the tumor growth curves and perform quantitative analysis based on the area under each curve.

Ethical statement

The design, methods, and protocol for the animal-related experiments in this work were conducted in accordance with the U.K. Animals Act, 1986 (Scientific Procedures) related guidelines. They were reviewed and approved by the Institutional Animal Care and Usage Committee of the Fifth Medical Center of General Hospital of Chinese PLA (approval ID: IACUC-2021-0026).

Statistical analysis

Data were presented as means ± standard deviations based on at least three biological replicates. The one-way analysis of variance (ANOVA) was used for statistical

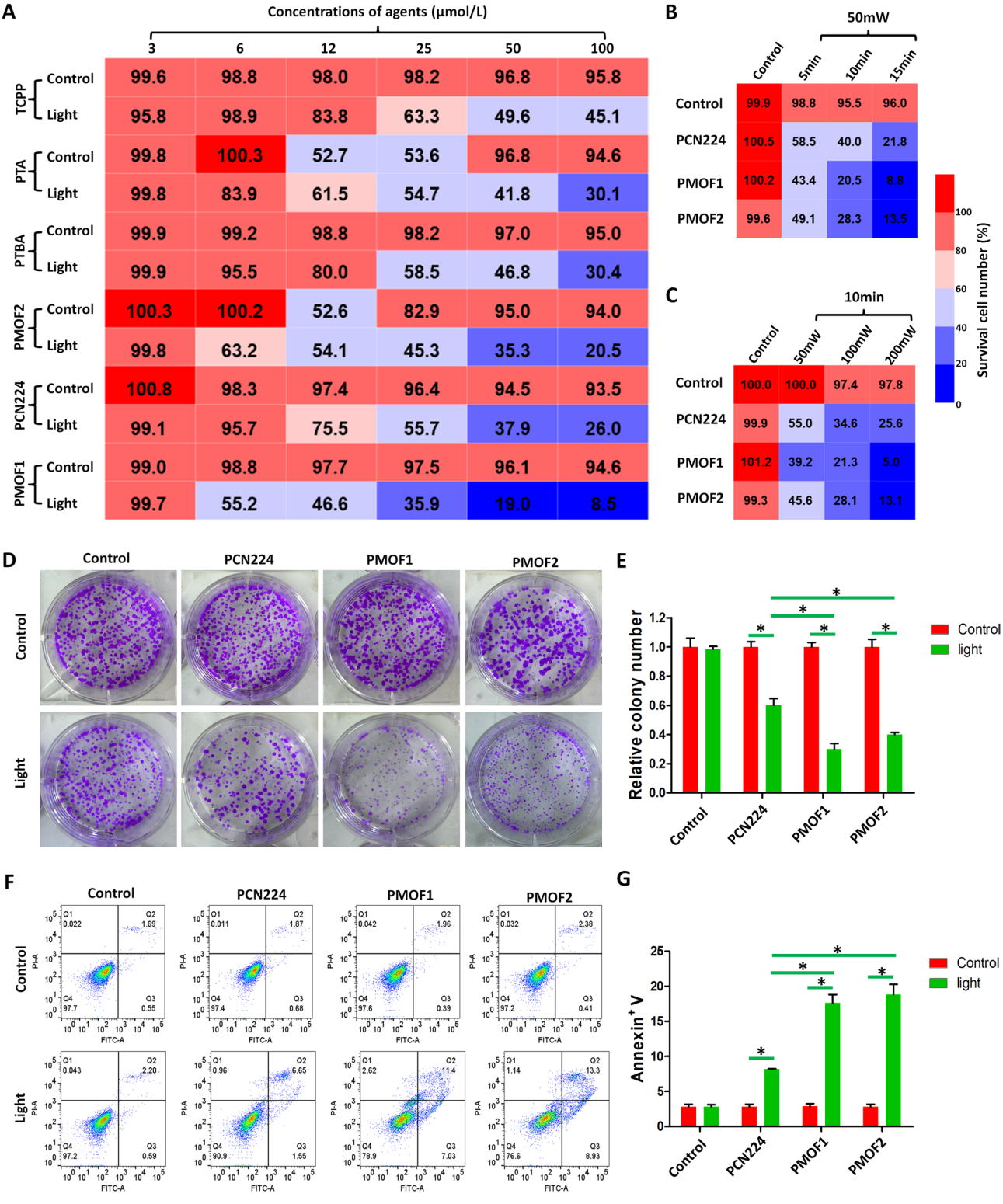

Fig. 2 (See legend on next page.)

analysis across various groups. Differences were considered statistically significant when $p < 0.05$.

Results

Synthesis of new porphyrin compounds

First, as illustrated in Fig. 1, we prepared the new porphyrin compounds PTA (Fig. 1a) and PTBA (Fig. 1b).

(See figure on previous page.)

Fig. 2 Antitumor Activity of TCPP, PTA, PTBA, PCN224, PMOF1, and PMOF2 on H520 Cells. H520 cells were cultured and treated as follows: (**A**) The cells were treated with the indicated concentrations (3, 6, 12, 25, 50, 100 μmol/L) of TCPP, PTA, PTBA, PCN224, PMOF1, and PMOF2 for 24 h. Then, the cells were exposed to a laser at 100 mW/cm^2. (**B**) The cells were treated with 100 μmol/L of PCN224, PMOF1, and PMOF2 for 24 h. Then, the cells were exposed to a laser at 50 mW/cm^2 for 5, 10, or 15 min. (**C**) The cells were treated with 100 μmol/L of PCN224, PMOF1, and PMOF2 for 24 h. Then, the cells were exposed to a laser at 50, 100, or 200 mW/cm^2 for 10 min. For all treatments (**A**-**C**), 24 h after laser exposure, the cells were analyzed by MTT assays. The survival cell number (proportion [%]) was calculated based on O.D. 490 nm values. The results were displayed as heatmap images according to the survival cell number. (**D** and **E**) The cells were treated with 100 μmol/L of PCN224, PMOF1, and PMOF2 for 24 h. Then, the cells were exposed to a laser at 100 mW/cm^2 for 10 min. The cells were analyzed by colony formation. The results were displayed as images of colonies (**D**) and quantitative results of colony images (**E**). (**F** and **G**) The cells were treated with 100 μmol/L of PCN224, PMOF1, and PMOF2 for 24 h. Then, the cells were exposed to a laser at 100 mW/cm^2 for 10 min. The cells were analyzed by flow cytometry for apoptosis. The results were displayed as images of Annexin V/7-AAD staining (**F**) and quantitative results of Annexin V/7-AAD staining images (**G**). In the Annexin-V flow cytometry plots, the Q1, Q2, Q3, and Q4 quadrants represent: Q1: PI-positive/Annexin-V-negative (necrotic cells); Q2: PI-positive/Annexin-V-positive (late apoptotic cells); Q3: PI-negative/Annexin-V-positive (early apoptotic cells); Q4: PI-negative/Annexin-V-negative (viable/normal cells); The apoptotic rate is calculated as the sum of Q3 (early apoptosis) and Q2 (late apoptosis) (Q2 + Q3). (*$P < 0.05$)

Supplementary Figs. 1 and 2 depict the identified H spectrograms, respectively. Due to the ring current effect of the porphyrin macrocycle which generates strong shielding, porphyrin compounds exhibit distinctive NMR characteristics. As shown in Supplemental Figs. 1 and 2: the N-H signal of tetraphenylporphyrin appears at approximately – 2.80 ppm. However, the porphyrin N-H protons may undergo rapid exchange with solvent (e.g., trace water in deuterated DMSO), resulting in signal disappearance. The β-pyrrolic protons of porphyrins typically resonate between δ 8.8-9.0 ppm. The aromatic protons from phenyl or substituted aryl groups generally appear in the δ 7.0-8.5 ppm range. Compounds PTA and PTBA displayed all these characteristic porphyrin NMR features. The NMR data thus match the expected structures, confirming their successful synthesis.

Based on these preparations, we evaluated the photosensitive antitumor activities of the novel porphyrin compounds and TCPP. As shown in Fig. 2a, TCPP, PTA, and PTBA can inhibit the survival of LSCC cell H520 in a dose-dependent manner under laser irradiation, but they exhibit no antitumor activity when acting alone. Notably, the photosensitive antitumor activity of PTA and PTBA surpasses that of TCPP, with PTA demonstrating the highest activity among the three (Fig. 2a). These results confirm the successful preparation of two new porphyrin compounds with promising photosensitive and antitumor properties.

Preparation based on three kinds of nanoparticles

Given the less-than-ideal photosensitive activity of the porphyrin compounds under laser irradiation, we further prepared these compounds and metal ions as nanoparticles. The results indicated that PTA (Fig. 3a) and PTBA (Fig. 3b) could form nanoparticles (Fig. 3c and d) with 4-valent chromium ions. The nanoparticles formed by PTA and Zr^{4+} were named PMOF1, while those formed by PTBA and Zr^{4+} were named PMOF2. The particle size distribution of these nanoparticles was uniform and closely matched the size observed by SEM. For the UV-Vis and structural characterization of nanoparticles, as shown in Fig. 3e, UV-vis spectroscopy demonstrated distinct absorption profiles for the three nanoparticles (PCN224, PMOF01, and PMOF02). PCN224 exhibited a sharp Soret band at 420 nm, while PMOF01 and PMOF02 showed redshifted absorption maxima at 431 nm and 453 nm, respectively, indicative of structural variations in their porphyrin coordination environments. PXRD analysis (Fig. 3f) further revealed crystallographic differences among the materials. All three nanoparticles displayed approximately seven discernible diffraction peaks; however, significant variations in peak positions (2θ values) and relative intensities confirmed their unique crystalline lattices. Fluorescence spectroscopy (Fig. 3g) highlighted emission maxima at 661 nm (PCN224), 692 nm (PMOF01), and 704 nm (PMOF02). These progressively redshifted emission bands correlate with modifications in the electronic band structures and surface defect states arising from their distinct metal-organic frameworks.

Additionally, Fig. 3h demonstrates that the absolute values of the zeta potential for the three metalloporphyrin compounds (PCN224, PMOF1, and PMOF2) are substantial (-18.3, -14.2, and – 19.8, respectively). The particle size distribution of these nanoparticles was relatively uniform, with noticeable differences in their sizes (Fig. 3i). Taking PMOF1 as an example, no significant change in particle size was observed after 72 h of storage in solution, indicating that the prepared nanoparticle dispersion system is relatively stable (due to the large absolute value of the zeta potential) and resistant to aggregation, with very stable particle sizes.

Photodynamic properties of porphyrin metal nanoparticles

Based on the previous results, porphyrin compounds were successfully synthesized into metal nanoparticles, and their photodynamic properties were further evaluated. As illustrated in Fig. 4a-d, the prepared nanoparticles generate ROS (reactive oxygen species) and singlet oxygen under laser irradiation. Notably, PMOF1 and PMOF2 released significantly higher levels of ROS and singlet oxygen compared to PCN224 under laser irradiation, with PMOF1 performing better than PMOF2. Furthermore, in H520 cells, laser irradiation following

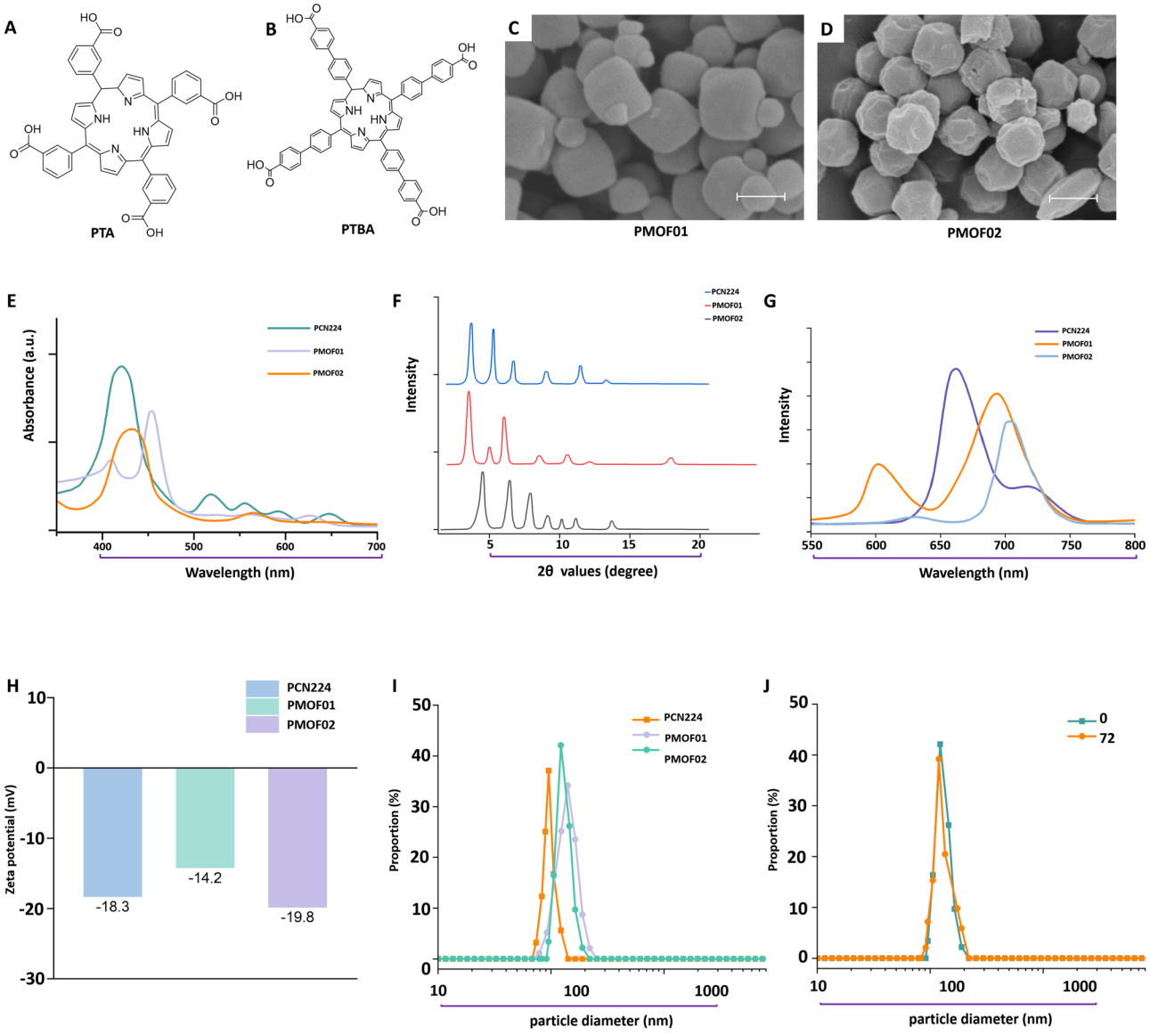

Fig. 3 The Physicochemical Properties of PMOF1 and PMOF2. The porphyrins PTA (**A**) and PTBA (**B**) were prepared as metal-nanoparticles named PMOF1 and PMOF2 (**B**). The structure and morphological characteristics of PMOF1 (**C**) and PMOF2 (**D**) were shown as SEM images. (**E**) The results of UV spectra, (**F**) PXRD spectra, and (**G**) fluorescence spectra of PCN224, PMOF1, and PMOF2 were displayed. (H) The absolute values of zeta potential of the three metal-loporphyrin nanoparticles were shown as bar-chart images. (**I** and **J**) The particle size distribution of the three nanoparticles was displayed. The scale-bar of the SEM images is 100 nm

treatment with these three types of nanoparticles induced ROS production (Fig. 4e-j). Specifically, PMOF1 (Fig. 4i and j) and PMOF2 (Fig. 4g and h) released significantly higher ROS levels than PCN224 (Fig. 4e and f) under laser irradiation, with PMOF1 again outperforming PMOF2. Both cell-free and intracellular results demonstrated that PMOF1 and PMOF2 exhibited superior photodynamic activities compared to PCN224.

Cellular uptake and tissue retention of porphyrin metal nanoparticles

The uptake of TCPP, PTA, PTBA, PCN224, PMOF1, and PMOF2 by H520 cells was investigated in cultured cells. As shown in Fig. 5a, H520 cells gradually ingested TCPP, PTA, and PTBA over time, but the uptake rate was limited. At 48 h, only about 4% of the porphyrin compounds were ingested by H520 cells (4.21 ± 0.05% for TCPP, 4.36 ± 0.15% for PTA, and 3.92 ± 0.15% for PTBA). However, preparing TCPP, PTA, and PTBA as nanoparticles significantly enhanced their uptake by H520 cells. At various time points, the uptake ratio of these nanoparticles

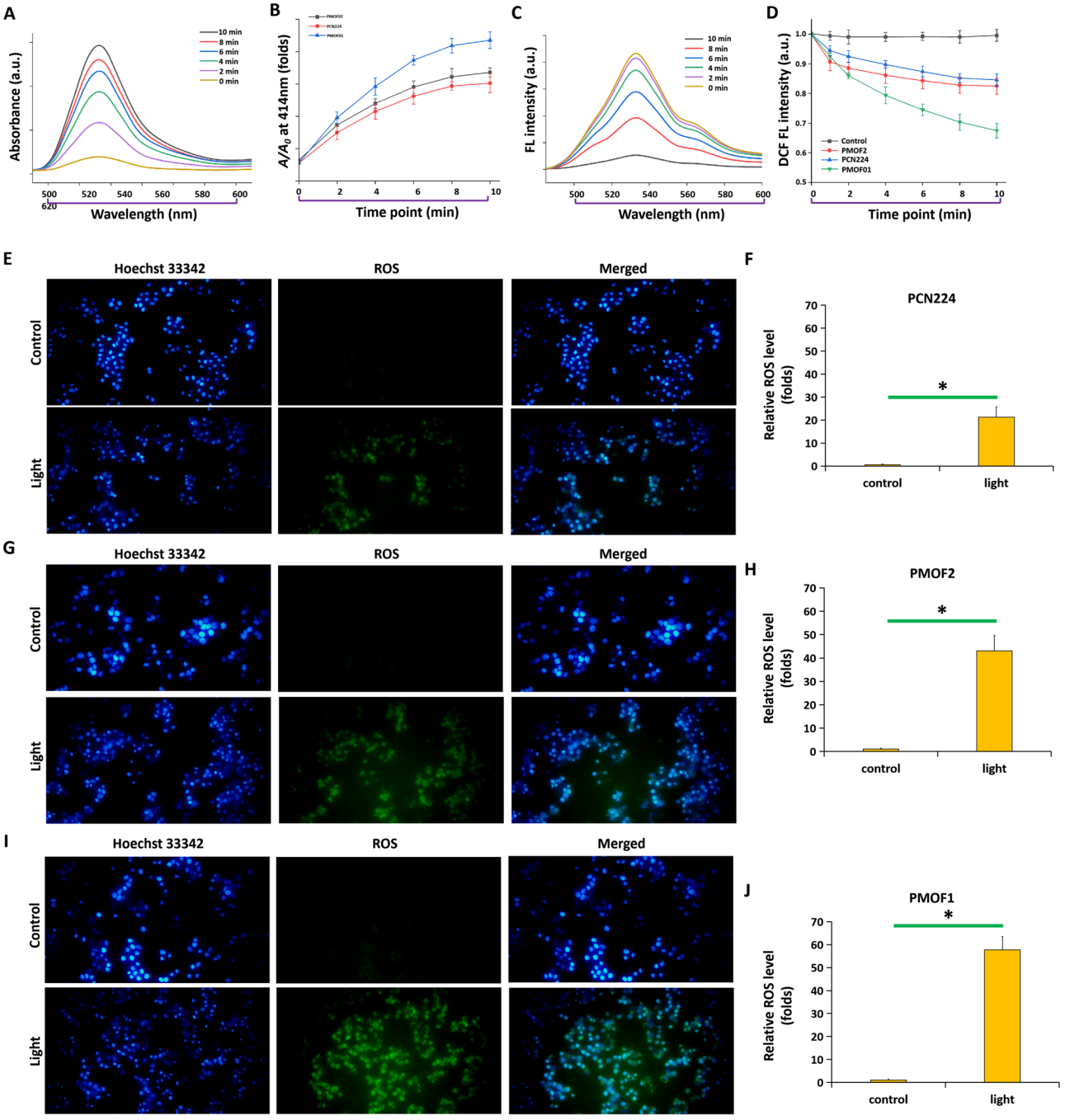

Fig. 4 The Photodynamic Activity of PCN224, PMOF1, and PMOF2. (**A**) Quantitative analysis of UV-Vis spectroscopy of PMOF1 in the singlet oxygen detection at various time points within 0–10 min. (**B**) Absorption intensity of UV-Vis spectroscopy of PCN224, PMOF1, and PMOF2 at 414 nm. (**C**) Quantitative analysis of fluorescence spectra of PCN224, PMOF1, and PMOF2 in ROS detection at various time points within 0–10 min. (**D**) Absorption intensity at 523 nm for fluorescence spectra of PCN224, PMOF1, and PMOF2 after incubation for different times. (**E**-**G**) H520 cells were treated with 100 μmol/L of PCN224, PMOF1, and PMOF2 for 24 h. Then, the cells were exposed to a laser at 100 mW/cm^2 for 10 min. The cells were analyzed by cell fluorescence staining. Blue fluorescence was excited using ultraviolet light (excitation wavelength 350 nm, emission wavelength 460 nm); blue fluorescence was used to excite green fluorescence (excitation wavelength 460 nm, emission wavelength 590 nm). The results are displayed as fluorescent photos (**E**, **G**, and **I**), with blue fluorescence indicating the nucleus and green fluorescence indicating ROS in the cytoplasm. Quantitative analysis of the obtained images was performed using ImageJ software (**F**, **H**, and **J**). The microscopic magnification in Fig. 4 is 400×. (*$P < 0.05$)

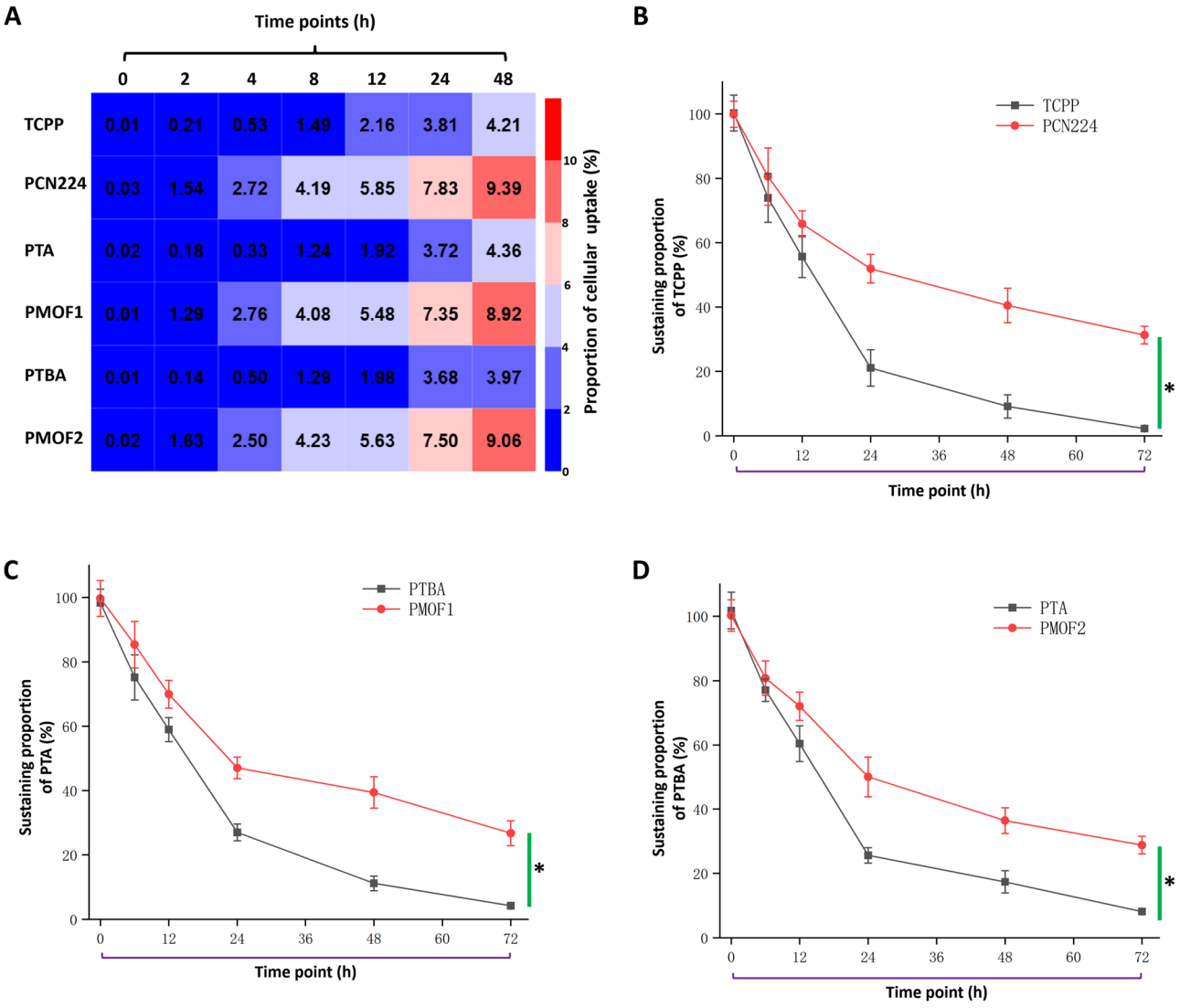

Fig. 5 Detection of Cellular Uptake and Retention of Metal Nanoparticles in Tumor Tissues. (**A**) Cellular Uptake Study: H520 cells were treated with a 100 μmol/L concentration of PCN224, PMOF1, and PMOF2 for the indicated time points (0, 2, 4, 8, 12, 24, and 48 h). Cells were collected at each time point, and the amount of TCPP, PTA, or PTBA in the cells was measured by LC-MS/MS. The total amount of porphyrins in the cells at each time point was calculated and normalized to the total amount of porphyrins in the cell culture medium (calculated based on the total volume and concentration of the medium) to obtain the cell uptake rate (%). A heatmap was generated based on these cell uptake rates. (**B**-**D**) Tumor Tissue Retention Study: H520 cells were cultured and injected into nude mice to form subcutaneous tumor tissues. When the tumor volumes reached 500 mm^3, solutions of TCPP or PCN224 (**B**), PTA or PMOF1 (**C**), and PTBA or PMOF2 (**D**) were directly injected into the subcutaneous tumor tissues. Tumor tissues were collected at the indicated time points (0, 12, 24, 36, 48, 60, and 72 h). The amount of TCPP (**B**), PTA (**C**), or PTBA (**D**) in each tumor tissue was measured by LC-MS/MS. The results were presented as retention curves of porphyrin. *$P < 0.05$

by H520 cells was significantly higher than that of the simple porphyrin compounds. For example, at the 48-hour time point, the proportions of PCN224, PMOF1, and PMOF2 in the total cell culture medium were 9.38 ± 0.07%, 8.92 ± 0.22%, and 9.05 ± 0.10%, respectively. These findings indicate that the preparation of metal nanoparticles based on porphyrin compounds facilitates their uptake by cells.

The retention of TCPP, PTA, PTBA, PCN224, PMOF1, and PMOF2 in tumor tissues was further examined. Tumor tissues were formed by subcutaneous inoculation of H520 cells in nude mice and injected with the compounds. The tumor tissues were collected at various time points to detect the content of TCPP, PTA, and PTBA. As shown in Fig. 5b-d, TCPP, PTA, and PTBA were gradually metabolized and eliminated in the tumor tissues, with nearly complete elimination occurring at 72 h. However, preparing TCPP, PTA, and PTBA into PCN224, PMOF1, and PMOF2 significantly prolonged their retention time in the tumor tissues. Specifically, a considerable proportion of TCPP, PTA, and PTBA remained in the tumor tissues at 72 h (Fig. 5b-d). These results suggest

that the preparation of metal nanoparticles based on porphyrin compounds is beneficial for extending the survival time of TCPP, PTA, and PTBA in tumor tissues.

Sensitization effect of nanoparticles on LSCC cells irradiated by laser

The antitumor activities of TCPP, PTA, PTBA, PCN224, PMOF1, and PMOF2 were further examined in detail. First, as shown in Fig. 2a, the prepared nanoparticles (PMOF1 and PMOF2) exhibited no significant cytotoxicity but could inhibit the survival of H520 cells in a dose-dependent manner when exposed to laser irradiation. Under laser irradiation, PMOF1 and PMOF2 showed a significantly higher inhibition rate on H520 cells compared to PCN224, with PMOF1 demonstrating superior antitumor activity to PMOF2. The power and duration of laser irradiation were further refined, as illustrated in Fig. 2b and c. The nanoparticles exhibited antitumor activity under various laser irradiation conditions, with PMOF1 and PMOF2 continuing to outperform PCN224 in inhibiting H520 cells. Considering both the results from Fig. 2A and the solubility characteristics of porphyrin compounds, we ultimately selected 100 μmol/L porphyrin concentration for subsequent experiments. Through integrated analysis of Fig. 2B and C, we adopted the intermediate parameter combination of 100 mW/cm² power density with 10-minute irradiation. Notably, this parameter setting (100 mW/cm² for 10 min) represents the most widely adopted configuration in comparable studies worldwide.

Based on the MTT assay, additional experiments, including cell apoptosis and cell colony formation assays, were conducted. As shown in Fig. 2d and e H520 cells pretreated with PCN224, PMOF1, and PMOF2 showed a significant decrease in the number and size of colonies formed after laser irradiation. The inhibition rate of colony formation by PMOF1 and PMOF2 was higher than that of PCN224, with PMOF1 exhibiting superior antitumor activity (Fig. 2d and e, Supplemental Fig. 3 and Supplemental Fig. 4). Similar results were observed in the cell apoptosis experiment (Fig. 2f and g): laser irradiation induced apoptosis in H520 cells pretreated with the nanoparticles, with PMOF1 and PMOF2 showing a significantly higher apoptosis rate than PCN224. These findings suggest that PMOF1 has great potential for application in photodynamic antitumor therapy.

In vivo antitumor activity of nanoparticles on lung squamous cell carcinoma cells

The above results were obtained using cultured cell lines. Therefore, a subcutaneous tumor model in nude mice was established for further investigation. As shown in Figs. 6 and 7, H520 cells successfully formed tumor tissue subcutaneously in nude mice. First, PCN224, PMOF1, and PMOF2 were injected into the tail vein of nude mice, followed by laser irradiation of the subcutaneous tumors. As illustrated in Figs. 6a-e, neither laser irradiation alone nor intravenous injection of nanoparticles (including low-dose and high-dose groups) had antitumor activity against the subcutaneous tumor formation of H520 cells. However, under laser irradiation, all three nanoparticles demonstrated antitumor activity, with the high-dose group showing significantly higher antitumor activity than the low-dose group. Notably, PMOF1 outperformed PMOF2 and PCN224, with tumor growth almost stopping after PMOF1 illumination. Tail vein injection of metal nanoparticles and laser irradiation had no effect on body-weight, main organ weight and main blood routine indexes of nude mice (Supplementary Tables 1 and 3).

Furthermore, when the nanoparticles were injected directly into the tumor tissue and then irradiated with laser, as shown in Figs. 7a-e, injection alone had no significant antitumor activity. However, combined with laser irradiation, a significant inhibition of subcutaneous tumorigenicity of H520 cells was observed. Tumor growth significantly slowed down after laser irradiation, with the high-dose group showing higher antitumor activity than the low-dose group. Again, PMOF1 demonstrated superior antitumor activity compared to PMOF2 and PCN224. Tumor growth stagnated after PMOF1 illumination, with the tumor tissue volume gradually shrinking over time. Intra-tumor injection of metal nanoparticles and laser irradiation had no effect on body-weight, main organ weight and main blood routine indexes of nude mice (Supplementary Tables 2 and 4).

These results further confirm that PMOF1 has excellent potential for application in photodynamic antitumor therapy.

Inhibitory activity of prepared nanoparticles on other malignant tumor cells

This study concentrated on the photodynamic therapy of lung squamous cell carcinoma, with the majority of results obtained using H520 cells. To investigate whether PTA, PTBA, PMOF1, and PMOF2 exhibit broad-spectrum anti-tumor activity, various human malignant tumor cell lines were further examined. Specifically, lung cancer cell lines such as A549 (lung adenocarcinoma) and H446 (small cell lung cancer) were included.

The results, presented in Fig. 8a and b, indicate that PCN224, PMOF1, and PMOF2 alone did not inhibit the survival of A549 cells (Fig. 8a) or H446 cells (Fig. 8b, note: originally referenced as Fig. 5b, corrected to Fig. 8b for consistency). However, under laser irradiation, these nanoparticles could kill A549 and H446 cells in a dose-dependent manner. Similar results were observed in additional cell lines, including H460, HepG2, Lovo, SW480, TT, BHT-101, KTC-1, B-CPAP, KYSE70, KYSE140,

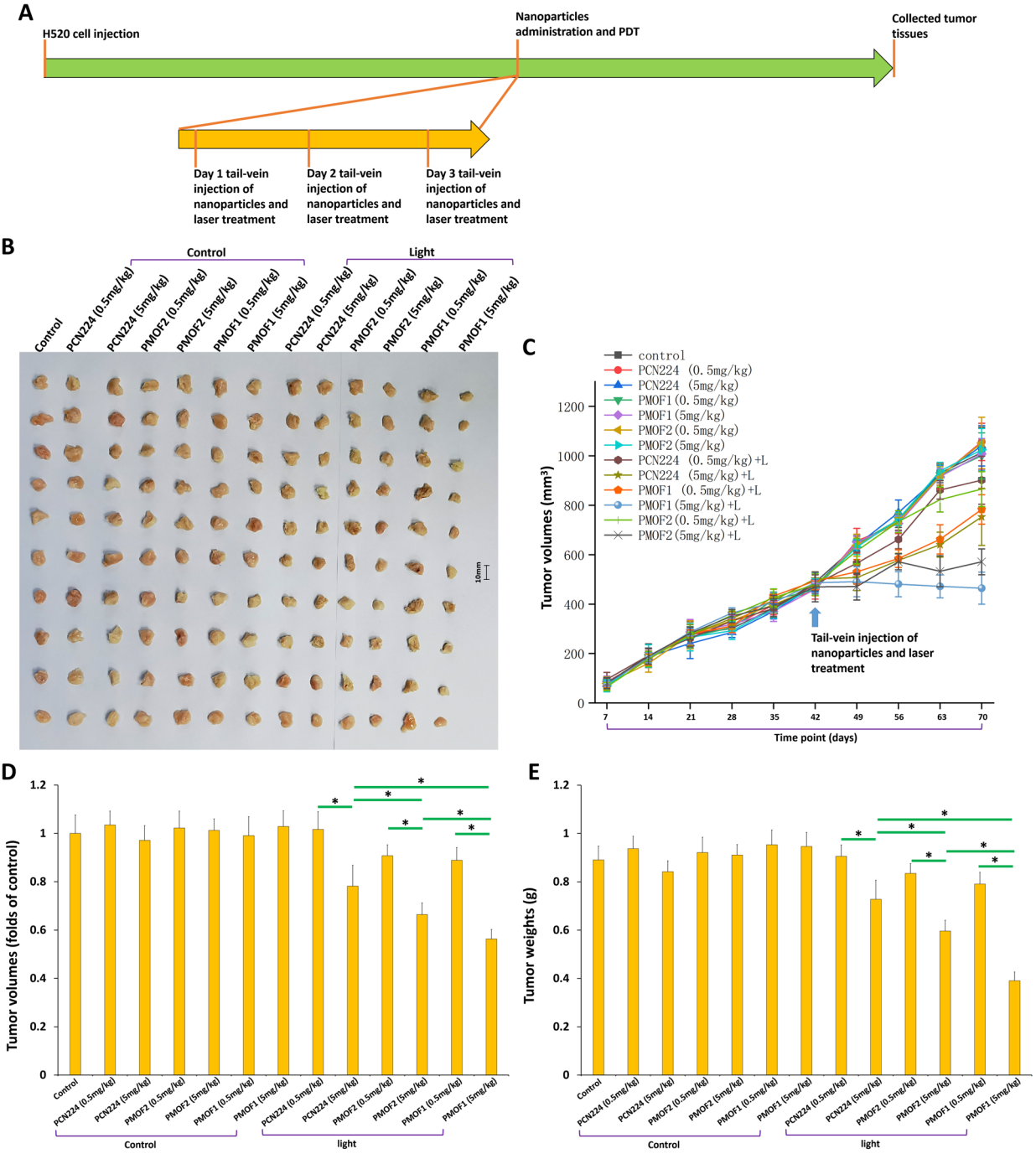

Fig. 6 Photosensitive Antitumor Activity of Metal Nanoparticles via Tail-Vein Injection. H520 cells were cultured and injected into nude mice to form subcutaneous tumor tissues. When the tumor volumes reached 500 mm^3, the mice were administered PCN224, PMOF1, or PMOF2 via tail-vein injection and the tumor tissues were treated with laser irradiation. The specific scheme was as follows: two doses (high dose: 5 mg/kg, low dose: 0.5 mg/kg) of the nanoparticles, laser irradiation at 100 mW/cm^2, administered once a day by intra-tumor injection, with laser irradiation conducted five hours after administration, for a total of three treatments. (**A**) Description of the experimental scheme. (**B**) Images of subcutaneous tumor tissues. (**C**) Tumor tissue volume was recorded, and the tumor growth curve was plotted. (**D**) Quantitative analysis of the tumor growth curve, with the area under the curve calculated using ImageJ software. The histogram was normalized to the control group. (**E**) Tumor tissues were collected and weighed at the end of the experiment. $N = 10$; $^*P < 0.05$

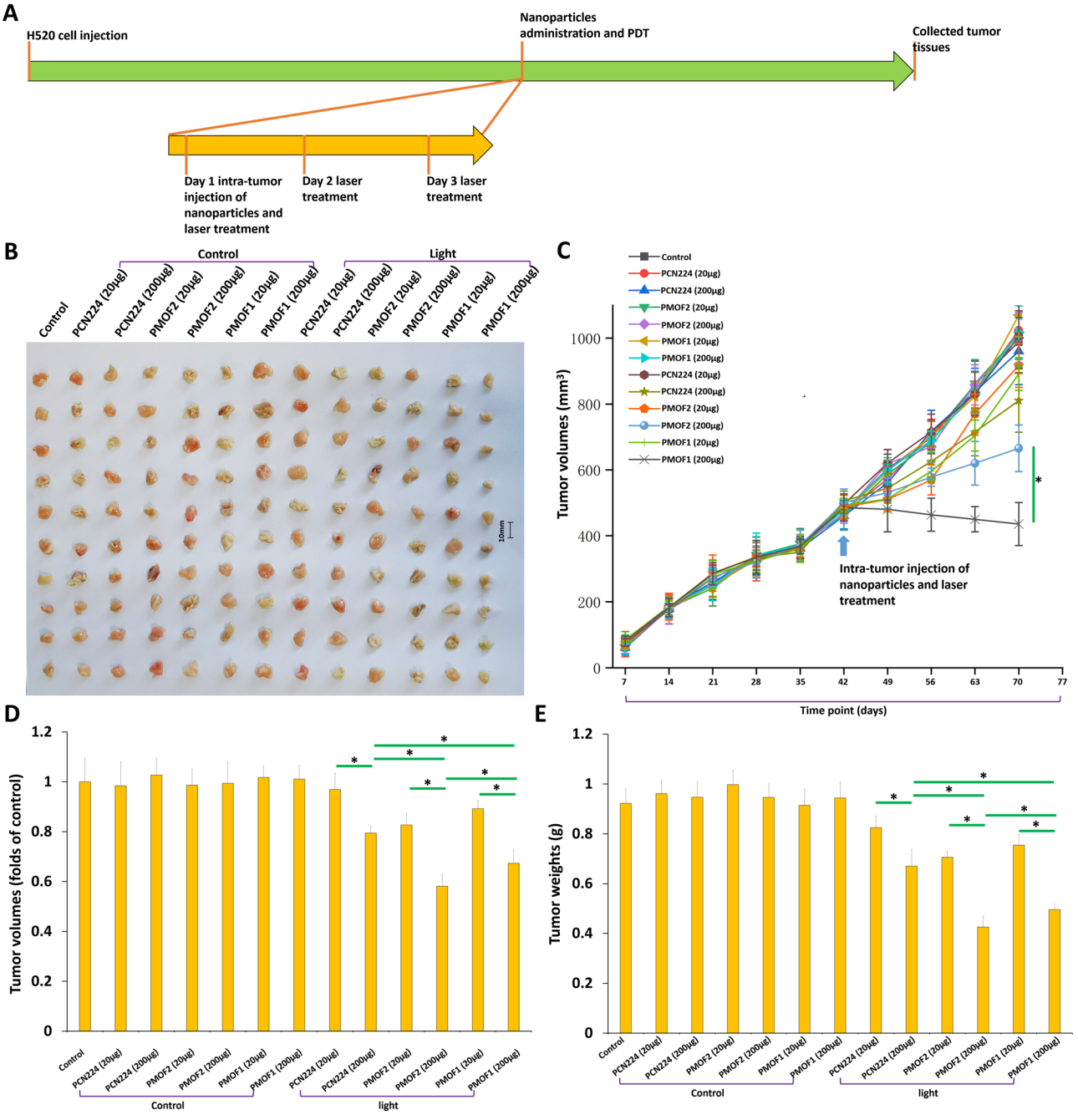

Fig. 7 Photosensitive Antitumor Activity of Metal Nanoparticles via Intra-Tumor Injection. H520 cells were cultured and injected into nude mice to form subcutaneous tumor tissues. When the tumor volumes reached 500 mm^3, the mice were administered PCN224, PMOF1, or PMOF2 via intra-tumor injection and the tumor tissues were treated with laser irradiation. The specific scheme was as follows: two doses (high dose: 200 μg, low dose: 20 μg; each tumor tissue injected with 20 μl of nanoparticle solution at 10 mg/ml for the high dose group and 1 mg/ml for the low dose group), laser irradiation at 100 mW/cm^2, administered once for intra-tumor injection, with laser irradiation conducted five hours after drug administration, and once a day for the next two days. (**A**) Description of the experimental scheme. (**B**) Images of subcutaneous tumor tissues. (**C**) Tumor tissue volume was recorded, and the tumor growth curve was plotted. (**D**) Quantitative analysis of the tumor growth curve, with the area under the curve calculated using Image J software. The histogram was normalized to the control group. (**E**) Tumor tissues were collected and weighed at the end of the experiment. $N = 10$; $^*P < 0.05$

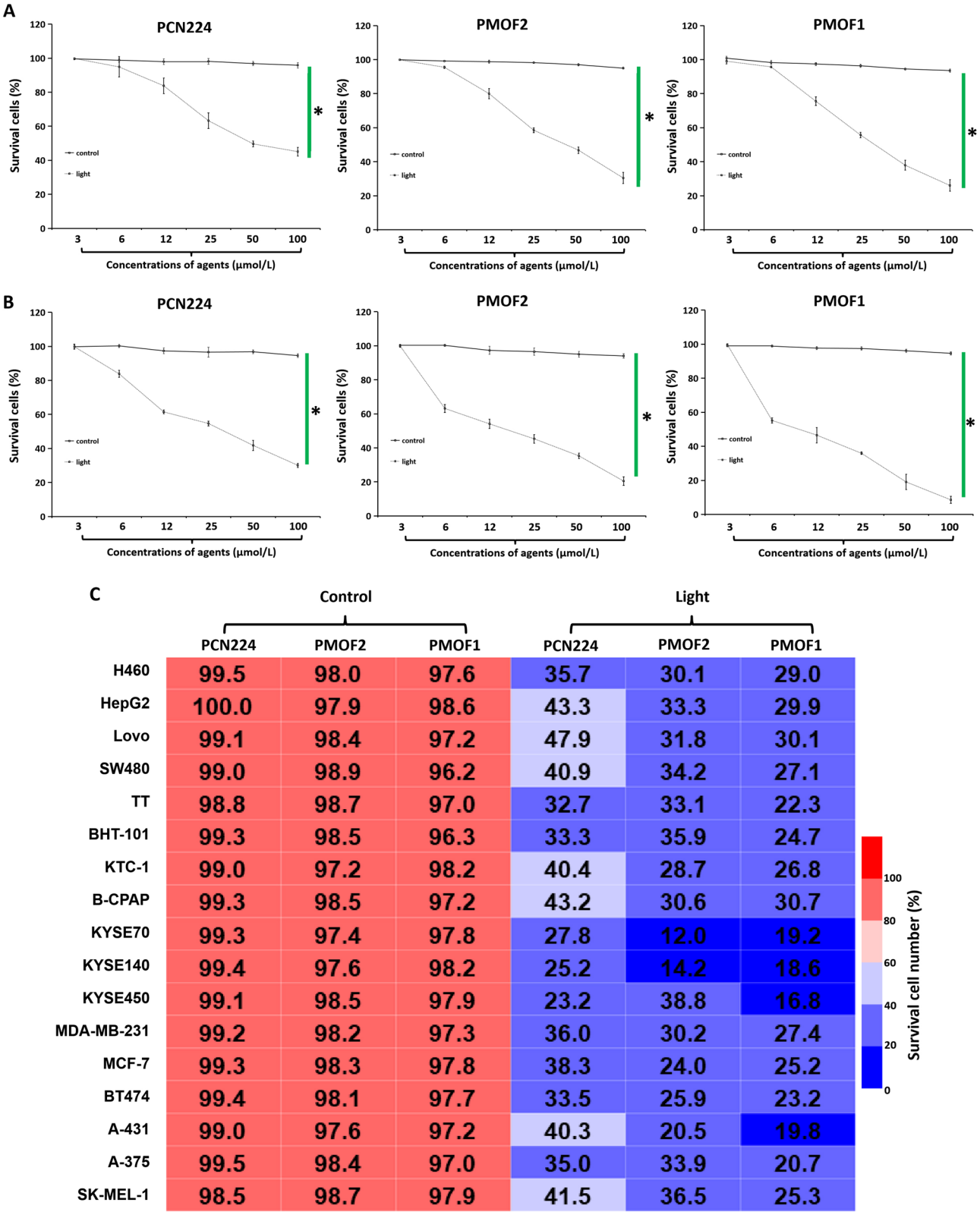

Fig. 8 (See legend on next page.)

(See figure on previous page.)

Fig. 8 Antitumor Activity of Metal Nanoparticles Against Various Cell Lines. (**A**) Lung Adenocarcinoma Cell Line: Cells were treated with the indicated concentrations (3, 6, 12, 25, 50, 100 μmol/L) of PCN224, PMOF1, or PMOF2 for 24 h, followed by laser irradiation at 100 mW/cm^2 for 10 min. Cell viability was analyzed by MTT assay 24 h later. Effect-dose curves were obtained based on the cell survival number determined by OD 490 nm. (**B**) Small Cell Lung Cancer Cell Line H446: Cells were treated similarly to the lung adenocarcinoma cell line and analyzed by MTT assay. (**C**) Various Cell Lines: H460, HepG2, Lovo, SW480, TT, BHT-101, KTC-1, B-CPAP, KYSE70, KYSE140, KYSE450, MDA-MB-231, MCF-7, BT474, A-431, A-375, and SK-MEL-1 cells were treated with a 100 μmol/L dose of PCN224, PMOF1, or PMOF2 for 24 h, followed by laser irradiation at 100 mW/cm^2 for 10 min. Cell viability was analyzed by MTT assay 24 h later. The results were presented as a heatmap based on the cell survival number (proportion [%]). *$P < 0.05$

KYSE450, MDA-MB-231, MCF-7, BT474, A-431, A-375, and sk-mel-1 (Fig. 8C). Across these cell lines, the order of antitumor activity was PMOF1 > PMOF2 > PCN224. These findings suggest that the prepared nanoparticles do not demonstrate cell type specificity.

Discussion

In this study, we modified the structure of TCPP, a commonly used porphyrin compound, by introducing phenyl or triphenylamine groups, resulting in two new porphyrin compounds: PTBA and PTA. Compared to TCPP, the structural modifications in PTBA and PTA enhance the internal conjugation of the porphyrin structure, which boosts π-π stacking and facilitates electron transfer, leading to a more effective phototherapeutic effect. The results of our study align with expectations, demonstrating that porphyrin is a key compound in phototherapy, and the structurally modified porphyrin compounds exhibit superior photosensitive activity compared to TCPP. Porphyrin compounds can form coordination bonds with metal ions to create nanoparticles. The interaction between metal ions and porphyrin compounds enhances the photosensitive activity of the porphyrins. In this study, TCPP, PTA, PTBA, and tetravalent Zr^{4+} ions were used to create metal nanoparticles (PCN224, PMOF1, and PMOF2). The interaction between porphyrins and metal ions significantly boosts their photosensitive activity. Notably, the phenyl or triphenylamine structures introduced into PTBA and PTA through structural modification facilitate their interaction with metal ions, potentially contributing to the superior photosensitive and antitumor activities of PMOF1 and PMOF2 compared to PCN224. It's worth mentioning that porphyrin compounds can form nanoparticles with various metal ions, each resulting in different structures [25]. For instance, porphyrin combined with divalent copper or zinc ions forms needle-like or sheet-like nanoparticles [15, 25]. In contrast, the metal nanoparticles formed by tetravalent Zr^{4+} ions and porphyrin in this study resemble a "cage" or "network" structure, typical of metal-organic frameworks (MOFs) [15, 25]. As a coordination polymer, MOFs offer advantages such as a porous structure, good biocompatibility, a large specific surface area, and ease of modification, making them widely used in catalysis, energy storage, separation, biomedicine, and other fields. Our previous research used PCN224 to load the mTOR inhibitor PKI587, pioneering a strategy that combines photodynamic therapy and sensitization on the same material [25]. Another breakthrough in this study is the use of insoluble small molecule inhibitors likePKI-587, [35, 36] expanding beyond previously used drugs with good solubility and permeability like doxorubicin. Based on the results of this study, we aim to explore whether PMOF1 and PMOF2 offer advantages over PCN224 in terms of both photosensitive activity and drug loading capacity. In summary, based on our findings and the current research landscape (both domestic and international), the superior antitumor efficacy of the as-prepared nanoparticles PMOF1 and PMOF2 may originate from the following three aspects: (1) the optimized chemical structures of PTA and PTBA compared to TCPP; (2) the formation of nanoparticles with tetravalent metal ions, wherein the metal ions significantly enhance the photosensitizing activity of porphyrins; (3) the nanoparticle formulations not only exhibit improved cellular uptake efficiency but also demonstrate prolonged retention time in tumor tissues when compared to free porphyrin compounds.

It is worth noting that this study primarily relies on Photodynamic Therapy (PDT). Alongside PDT, Photothermal Therapy (PTT) also holds significant importance. In PTT, a photosensitive material is irradiated by laser, converting the absorbed photon energy into heat energy [37, 38]. This rapidly elevates the local cell temperature above the threshold of 42–45 °C within a specific timeframe, effectively ablating cancer cells [37, 38]. Further exploration is necessary, particularly regarding the use of TCPP, PTA, and PTBA in PTT, and whether special chemical structure modifications are required. Both microwave ablation and radiofrequency ablation are thermal ablation strategies with substantial theoretical and practical value in anti-tumor diagnosis and treatment, albeit with differing mechanisms [39–42]. PTT serves as a potent supplement to these ablation methods. When combined with molecular targeted drugs or immune checkpoint inhibitors, microwave ablation and radiofrequency ablation offer clear clinical benefits to patients. Similarly, PTT, when loaded with small molecular drugs for collaborative treatment, can compensate for its limitations and significantly enhance the anti-tumor effect.

In this study's animal experiments, both tail vein injection and intratumor injection were employed. Tail vein injection represents systemic chemotherapy, whereas

intratumoral injection mimics the precise drug delivery strategy of interventional therapy at the animal experimental level [43]. Techniques such as Transcatheter Arterial Chemoembolization (TACE) guided by Digital Subtraction Angiography (DSA) and other medical images facilitate minimally invasive and precise treatment [44]. For instance, CT-guided percutaneous puncture allows direct injection of drugs into tumor tissue [44 However, existing drugs do not fully exploit the advantages of interventional therapy. Lipiodol, primarily used in TACE, or mixed with Adriamycin or platinum drugs and deposited in HCC tissue, gradually detaches due to blood flow. Adriamycin's excellent water solubility prevents complete mixing with lipiodol, and its presence in tumor tissue after TACE is limited [45]. Platinum drugs, containing metal ions, are more challenging to mix than Adriamycin and lipiodol, impeding the full benefits of their combination. Current drug-loaded embolic microspheres use porous polymer materials to physically adsorb doxorubicin or platinum drugs [46, [47]. Doxorubicin's water solubility complicates sustained drug release and long-term anti-tumor effects post-delivery [48, 49]. Platinum drugs' charged nature limits their adsorption efficiency by polymer materials, making it difficult to achieve simultaneous vascular occlusion, drug release, and precise delivery. In this study, regardless of the administration strategy, PMOF1 and PMOF2 exhibited no significant toxicity and had no impact on mice weight, organs, or blood routine. Only under laser irradiation can Metal-Organic Frameworks (MOF) serve as high-efficiency drug carriers, flexibly accommodating various drugs. Additionally, using poloxamer [50–52] and other polymer materials (such as CHITOSAN or hyaluronic acid) [53–57] to encapsulate MOF enables long-term, slow-release in tumor tissues. Poloxamer's temperature-sensitive properties (facilitating transport and preservation) form a gel under body temperature post-administration, also suitable for blood vessel embolization. Therefore, metal frame nanoparticles hold promising research and application prospects in the future.

This study focuses on lung squamous cell carcinoma, because the location of lung squamous cell carcinoma is easy to achieve tracheoscopic access, and various coaxial guide wires of tracheoscopy have also been used for drug administration and treatment. In addition to squamous cell carcinoma of the lung, a variety of other malignant tumor cells were also detected. The results of lung adenocarcinoma cell line A549, lung squamous cell carcinoma cell line H520, large cell lung cancer cell line H460 and small cell lung cancer cell line H446 showed that PMOF1 and PMOF2 had no case type specificity in the antitumor treatment of lung cancer. Some human superficial tumor cells, including MTC cell line TT; Thyroid cancer cell lines bht-101, KTC-1 and B-CPAP; Breast cancer cell lines MDA-MB-231, MCF-7 and BT474; Skin cancer cell line A-431; Melanoma cell lines a-375 and sk-mel-1. These superficial tumors are very suitable for laser irradiation, and the minimally invasive operation of intratumoral injection of drugs is also easy to achieve. Similar to lung squamous cell carcinoma, ESCC can be operated by esophagoscopy; [58, 59]. Colorectal cancer cells can be treated by colonoscopy [60, 61]. Although PMOF1 and PMOF2 also have good antitumor activity on hepatocellular carcinoma cell line HepG2, how to achieve effective photodynamic therapy for HCC needs further exploration.

Conclusion

In this study, two new porphyrin compounds were successfully synthesized and prepared as metal nanoparticles with good photosensitive anti-tumor activity. This not only expands our understanding of photodynamic therapy, but also helps to provide new treatment strategies for lung squamous cell carcinoma.

Abbreviations

PDT	Photodynamic therapy
NSCLC	Non-small cell lung cancers
LA	Lung adenocarcinoma
SCLC	Small cell lung cancer
LSCC	Lung squamous carcinomas
ROS	Reactive oxygen species
NIR	Near-infrared
TCPP-20	Tetrakis(4-carboxyphenyl)porphyrin
DPBF	1-diphenylisobenzofuran
DCFH-DA	2,7-dichlorofluorescein diacetate
DMSO	Dimethyl sulfoxide
DMF	N-dimethylformamide
PBS	Phosphate buffer solution
ESCC	Esophageal squamous cell carcinoma
LC-MS/MS	Liquid Chromatograph Mass Spectrometer
MOFs	Metal-organic frameworks
PTT	Photothermal Therapy
TACE	Transcatheter Arterial Chemoembolization

Supplementary Information

The online version contains supplementary material available at https://doi.org/10.1186/s12885-025-14386-4.

Supplementary Material 1

Supplementary Material 2

Supplementary Material 3

Supplementary Material 4

Supplementary Material 5

Supplementary Material 6

Supplementary Material 7

Supplementary Material 8

Acknowledgements

N.A.

Author contributions
S.M.W., S.Q.L. H.M., R.Q.D. and F.F. wrote the main manuscript text. H.M. and R.Q.D. prepared Figs. 1, 2, 3, 4, 5, 6, 7 and 8. L.J., X.P.C. and Y.H.H. prepared supplemental figures 1-4 and supplmental Tables 1, 2, 3 and 4. All authors reviewed the manuscript.

Funding
This work was supported by the Shenyang Science and Technology Plan Project (No. 24-214-3-119), and National Natural Science Foundation of China (No. 81702986).

Data availability
Data is provided within the manuscript or supplementary information files. All the data generated or analyzed in this study are included in the Materials and Methods section.

Declarations

Ethics approval and consent to participate
The design, methods, and protocol for the animal-related experiments in this work were conducted in accordance with the U.K. Animals Act, 1986 (Scientific Procedures) related guidelines. They were reviewed and approved by the Institutional Animal Care and Usage Committee of the Fifth Medical Center of General Hospital of Chinese PLA (approval ID: IACUC-2021-0026).

Consent for publication
Not applicable.

Competing interests
The authors declare no competing interests.

Received: 27 March 2025 / Accepted: 23 May 2025
Published online: 28 May 2025

References

1. GBD 2021 US Burden of Disease Collaborators. The burden of diseases, injuries, and risk factors by state in the USA, 1990–2021: a systematic analysis for the global burden of disease study 2021[J]. Lancet. 2024;404:2314–40.
2. Presley CJ, OWEN DH. Improved survival for patients with lung cancer treated with perioperative immunotherapy[J]. Lancet. 2024;404:1176–8.
3. Meyer ML, Fitzgerald BG, PAZ-ARES L, et al. New promises and challenges in the treatment of advanced non-small-cell lung cancer[J]. Lancet. 2024;404:803–22.
4. Chen W, Gao P, Lu F, et al. CT texture features of lung adenocarcinoma with HER2 mutation. BMC Cancer[J]. 2025;25:287.
5. Fukushima T, Katsusshima U, Ogushi N, et al. Lower-extremity muscle strength is associated with prognosis in patients with advanced or recurrent lung cancer: a retrospective, observational study[J]. BMC Cancer. 2025;25:282.
6. Henick BS, Taylor AM, Nakagawa H, Squamous cell cancers of the aero-upper digestive tract: A unified perspective on biology, genetics, and therapy[J]. Cancer Cell. 202;43:178–94.
7. Luo J, Bishop JA, Dubois SG, et al. Hiding in plain sight: NUT carcinoma is an unrecognized subtype of squamous cell carcinoma of the lungs and head and neck[J]. Nat Rev Clin Oncol. 2025;22:292–306.
8. Ghosh DD, Mcdonald H, Dutta R, et al. Prognostic indicators for precision treatment of Non-Small cell lung carcinoma. Cells. 2024;13:1785.
9. Li Z, Qin C, Yang X et al. Phthalocyanine and photodynamic therapy relieve albumin Paclitaxel and gemcitabine chemoresistance in pancreatic cancer. Exp Cell Res. 2025:114455.
10. Zhu J, Tian L. Mechanistic insights into NIR-II AIEgens boosted multimodal Phototheranostics[J]. Small. 2025;21:e2410441.
11. Zhou W, Feng F, Zhang J, et al. pH-Sensitive porphyrin Metal-Organic frameworks for controlled delivery of Para-Toluenesulfonamide and photodynamic Cancer Therapy[J]. Drug Des Devel Ther. 2025;19:2351–68.
12. Obaid G, Celli JP. Engineering photodynamics for treatment, priming and imaging. Nat Rev Bioeng. 2024;2:752–69.
13. Yu H, Huang Z, Wu J, et al. Chlorin e6: a promising photosensitizer of anti-tumor and anti-inflammatory effects in PDT. Nanomed (Lond)[J]. 2025;20:389–400.
14. Zhang J, Zhang A, Guo Y, et al. Nanoparticle-Mediated Cuproptosis and photodynamic synergistic strategy: A novel horizon for Cancer Therapy[J]. Cancer Med. 2025;14:e70599.
15. Feng Y, Wu W. Metal-organic frameworks for hepatocellular carcinoma therapy and mechanism[J]. Front Pharmacol. 2022;13:1025780.
16. Sang L, Yang S, Zhu Y, et al. The combined use of B vitamins and probiotics promotes B vitamin absorption and increases Akkermansia abundance[J]. Food Funct. 2024;15:7017–31.
17. Bandyopadhyay S, Forzano JA, et al. Activatable Porphyrin-Based sensors, photosensitizers and combination Therapeutics[J]. JACS Au. 2025;5:42–54.
18. Wegner H, Roitman S, Kupcozok A, et al. Identification of Shemin pathway genes for tetrapyrrole biosynthesis in bacteriophage sequences from aquatic environments[J]. Nat Commun. 2024;15:8783.
19. Jiang M, Wu S, Zhang H, et al. Twin-Tail Tadpole-Shaped Ce6-Peptide conjugate for enhanced photodynamic Cancer Therapy[J]. ACS Appl Bio Mater. 2025;8:1475–83.
20. De Bei O, Marchetti M. Time-resolved X-ray solution scattering unveils the events leading to hemoglobin Heme capture by Staphylococcal IsdB[J]. Nat Commun. 2025;16:1361.
21. Gallo Ruelas M, Alvarado-Gamarra G, et al. A comparative analysis of Heme vs non-heme iron administration: a systematic review and meta-analysis of randomized controlled trials[J]. Eur J Nutr. 2024;64:51.
22. Jun M, Vijayan V, Shin S, et al. A bleomycin-mimicking manganese-porphyrin-conjugated mitochondria-targeting peptoid for cancer therapy[J]. Bioorg Med Chem. 2025;117:118023.
23. Xie M, Jiang C, Zhang C, et al. Tumor microenvironment triggered iron-based metal organic frameworks for magnetic resonance imaging and photodynamic-enhanced ferroptosis therapy[J]. J Colloid Interface Sci. 2025;685:382–95.
24. Cai M, Fu T, Zhu R, et al. An iron-based metal-organic framework nanoplatform for enhanced ferroptosis and Oridonin delivery as a comprehensive antitumor strategy[J]. Acta Pharm Sin B. 2024;14:4073–86.
25. Feng Y, Jiang Q, Ma X, et al. Photosensitizing metal-organic framework nanoparticles combined with tumor-sensitization strategies can enhance the phototherapeutic effect upon medullary thyroid carcinoma[J]. Biochim Biophys Acta Gen Subj. 2024;1868:130725.
26. Tao X, Li S, Wu H, et al. Progress in the application of bronchoscopic cryotherapy in pediatric pulmonary Diseases[J]. Child (Basel). 2024;11:1130.
27. Velez A, Demaio A. Cryoablation and immunity in non-small cell lung cancer: a new era of cryo-immunotherapy[J]. Front Immunol. 2023;14:1203539.
28. Li B. Rhamnetin decelerates the elimination and enhances the antitumor effect of the molecular-targeting agent Sorafenib in hepatocellular carcinoma cells via the miR-148a/PXR axis[J]. Food Funct. 2021;12:2404–17.
29. Feng F, Jiang Q. Pregnane X receptor mediates Sorafenib resistance in advanced hepatocellular carcinoma[J]. Biochim Biophys Acta Gen Subj. 2018;1862:1017–30.
30. Zhao Z, Ma X, Li YM, et al. Combination antitumor activation of anlotinib with radiofrequency ablation in human medullary thyroid Carcinoma[J]. Curr Mol Med. 2024. https://doi.org/10.2174/0115665240323681241023100958. Online ahead of print.
31. Li P, Hu X. Novel potent molecular glue degraders against broad range of hematological cancer cell lines via multiple neosubstrates degradation[J]. J Hematol Oncol. 2024;17:77.
32. Hao J, Chen Q, Feng Y, et al. Combination treatment with FAAH inhibitors/URB597 and ferroptosis inducers significantly decreases the growth and metastasis of renal cell carcinoma cells via the PI3K-AKT signaling pathway[J]. Cell Death Dis. 2023;14:247.
33. Zhang Y, Li D, Jiang Q, et al. Novel ADAM-17 inhibitor ZLDI-8 enhances the in vitro and in vivo chemotherapeutic effects of Sorafenib on hepatocellular carcinoma cells[J]. Cell Death Dis. 2018;9:743.
34. Sun H, Feng F, Xie H, et al. Quantitative examination of the inhibitory activation of molecular targeting agents in hepatocellular carcinoma patient-derived cell invasion via a novel in vivo tumor model. Anim Model Exp Med. 2019;2:259–68.
35. Zeng M, Hu Y, Zhao L, et al. Design, synthesis, and Pharmacological evaluation of triazine-based PI3K/mTOR inhibitors for the potential treatment of non-small cell lung cancer[J]. Eur J Med Chem. 2025;284:117200.
36. Umemura S, Udagawa H, Ikeda T, et al. Clinical significance of a prospective large genomic screening for SCLC: the genetic classification and a Biomarker-Driven phase 2 trial of Gedatolisib[J]. J Thorac Oncol. 2025;20:177–93.

37. Wang Lh, Jiang Y, Sun CH, et al. Advancements in the application of ablative therapy and its combination with immunotherapy in anti-cancer therapy[J]. Biochim Biophys Acta Rev Cancer. 2025;1880:189285.
38. Tang L, Yang X. Preclinical advance in nanoliposome-mediated photothermal therapy in liver cancer[J]. Lipids Health Dis. 2025;24:31.
39. Sun J, Chang Zy, Gaio XD, et al. Novel nanoparticle CS-C60-Fe3O4 magnetically induces tissue-specific aggregation and enhances thermal ablation of hepatocellular carcinoma[J]. Cancer Nanotechnol. 2024;15:1–16.
40. Cui J, Sui X, Lliu K, et al. Radiofrequency ablation for peribiliary hepatocellular carcinoma: propensity score matching analysis[J]. Insights Imaging. 2025;16:45.
41. Zhou Hd, Wei Y, ZHAO ZL, et al. A clinical study on microwave ablation of T1N0M0 papillary thyroid carcinoma locating in dangerous region[J]. BMC Cancer. 2025;25:240.
42. Wang X, Sun X, Lei Y, et al. The efficacy and safety of radiofrequency ablation combined with lenvatinib plus sintilimab in unresectable hepatocellular carcinoma: a real-world study[J]. BMC Cancer. 2024;24:1036.
43. Feng F, Jiang Q, Jia H, et al. Which is the best combination of TACE and Sorafenib for advanced hepatocellular carcinoma treatment? A systematic review and network meta-analysis[J]. Pharmacol Res. 2018;135:89–101.
44. Friedman DD, Ponkowski MJ, Shetty AS, et al. CT angiography of the upper extremities: review of acute arterial Entities[J]. Radiographics. 2025;45:e240077.
45. Kuehnle RA, Tchlebi LT, Ludmir EB, et al. Meta-analysis of randomized controlled trials of external-beam radiation versus transarterial chemoembolization for hepatocellular carcinoma[J]. Cancer. 2025;131:e35720.
46. Hyang JX, Yang R, Long H, et al. Dual-drug loaded chondroitin sulfate embolization beads enhance TACE therapy for HCC by integrating embolization, chemotherapy, and anti-angiogenesis[J]. Mater Today Bio. 2024;30:101419.
47. Jin B, Gu Y. Efficacy of CalliSpheres() drug-loaded microspheres combined with doxorubicin in hepatocellular carcinoma[J]. Scand J Gastroenterol. 2024;59:1087–92.
48. Wang Q, Zhu L, Sheng Q. Clinical research progress of callisperes() of drug-loaded microsphere arterial chemoembolisation in the treatment of solid tumors[J]. Discov Oncol. 2024;15:161.
49. Xu A, Sun Y. Monodisperse polyaspartic acid derivative microspheres for potential tumor embolization Therapy[J]. Macromol Biosci. 2024;24:e2400047.
50. Wang TJ, Rethi L, Ku MY, et al. A review on revolutionizing ophthalmic therapy: unveiling the potential of Chitosan, hyaluronic acid, cellulose, cyclodextrin, and poloxamer in eye disease treatments[J]. Int J Biol Macromol. 2024;273:132700.
51. Higashi T, Taharabaru T. Synthesis of cyclodextrin-based Polyrotaxanes and polycatenanes for supramolecular pharmaceutical sciences[J]. Carbohydr Polym. 2024;337:122143.
52. Shriky B, Vigato AA, Sepulveda AF, et al. Poloxamer-based nanogels as delivery systems: how structural requirements can drive their biological performance[j]?[J]? Biophys Rev. 2023;15:475–96.
53. Yang D, Liu Q, Xu Q, et al. Effects of collagen hydrolysates on UV-induced Photoaging mice: Gly-Pro-Hyp as a potent anti-photoaging peptide[J]. Food Funct. 2024;15:3008–22.
54. Zhang L, Wang K, Liang S, et al. Beneficial effect of ζ-carotene-like compounds on acute UVB irradiation by alleviating inflammation and regulating intestinal flora[J]. Food Funct. 2023;14:8331–50.
55. Liu W, Liu YY, Zhang MQ, et al. A comparative study of the ameliorative effects of hyaluronic acid oligosaccharides and hyaluronic acid on DSS-induced colitis in mice and research on relevant mechanisms[J]. Food Funct. 2023;14:6482–95.
56. Yu X, Li G, Zhou S, et al. Glycosylation of oyster peptides by COS ameliorates zinc deficiency-induced syndromes: intestinal inflammation and imbalance of the gut microbiota in vivo[J]. Food Funct. 2025;16:640–56.
57. Semenova MG, Antipova AS, Martirosova EI. Key structural factors and intermolecular interactions underlying the formation, functional properties and behaviour in the Gastrointestinal tract in vitro of the liposomal form of nutraceuticals coated with Whey proteins and chitosan[J]. Food Funct. 2024;15:2008–21.
58. Ishihara R, Kawachi H, Nakano K, et al. Comprehensive pathological evaluation of risk factors for metastasis after endoscopic resection of superficial esophageal squamous cell carcinoma[J]. J Gastroenterol. 2025;60:131–40.
59. Shimizu R, Yoshio T, Hijikata K, et al. Characteristics of multiple esophageal squamous cell carcinomas detected in the surveillance after endoscopic resection[J]. Esophagus. 2025;22:115–23.
60. Farooq A, Bani Fawwaz B, Mian A, et al. Patient adherence to surveillance colonoscopy after endoscopic resection of colorectal polyps and factors associated with loss to follow-up[J]. Endosc Int Open. 2025;13:a24094916.
61. Sguiglia S, Volij C, Rodriguez-Tablado M, et al. Adherence to colorectal cancer screening in a private health insurance center in Argentina from 2008 to 2022[J]. Rev Peru Med Exp Salud Publica. 2025;41:405–10.

Publisher's note